CORA Cork Open Research Archive
Cartlann Taighde Oscailte Chorcaí

Title	Tissue-specific geometry and chemistry of modern and fossilized melanosomes reveal internal anatomy of extinct vertebrates
Authors	Rossi, Valentina;McNamara, Maria E.;Webb, Sam M.;Ito, Shosuke;Wakamatsu, Kazumasa
Publication date	2019-08-19
Original Citation	Rossi, V., McNamara, M. E., Webb, S. M., Ito, S. and Wakamatsu, K. (2019) 'Tissue-specific geometry and chemistry of modern and fossilized melanosomes reveal internal anatomy of extinct vertebrates', Proceedings of the National Academy of Sciences, 116(36), pp. 17880-17889. DOI: 10.1073/pnas.1820285116
Type of publication	Article (peer-reviewed)
Link to publisher's version	https://www.pnas.org/content/116/36/17880 - 10.1073/pnas.1820285116
Rights	©2019 the Author(s). Published by PNAS. This open access article is distributed under Creative Commons Attribution-NonCommercial-NoDerivatives License 4.0 (CC BY-NC-ND). - https://creativecommons.org/licenses/by-nc-nd/4.0/
Download date	2026-11-15 16:27:13
Item downloaded from	https://hdl.handle.net/10468/8770



University College Cork, Ireland
Coláiste na hOllscoile Corcaigh

Tissue-specific geometry and chemistry of modern and fossilized melanosomes reveal internal anatomy of extinct vertebrates

Valentina Rossi[a,1], Maria E. McNamara[a,1], Sam M. Webb[b], Shosuke Ito[c], and Kazumasa Wakamatsu[c]

[a]School of Biological, Earth and Environmental Sciences, University College Cork, T23 TK30 Cork, Ireland; [b]SLAC National Accelerator Laboratory, Stanford Synchrotron Radiation Lightsource (SSRL), Menlo Park, CA 94025; and [c]Department of Chemistry, Fujita Health University School of Health Sciences, 470-1192 Toyoake, Aichi, Japan

Edited by Roy A. Wogelius, University of Manchester, Manchester, United Kingdom, and accepted by Editorial Board Member David Jablonski July 3, 2019 (received for review November 28, 2018)

Recent discoveries of nonintegumentary melanosomes in extant and fossil amphibians offer potential insights into the physiological functions of melanin not directly related to color production, but the phylogenetic distribution and evolutionary history of these internal melanosomes has not been characterized systematically. Here, we present a holistic method to discriminate among melanized tissues by analyzing the anatomical distribution, morphology, and chemistry of melanosomes in various tissues in a phylogenetically broad sample of extant and fossil vertebrates. Our results show that internal melanosomes in all extant vertebrates analyzed have tissue-specific geometries and elemental signatures. Similar distinct populations of preserved melanosomes in phylogenetically diverse vertebrate fossils often map onto specific anatomical features. This approach also reveals the presence of various melanosome-rich internal tissues in fossils, providing a mechanism for the interpretation of the internal anatomy of ancient vertebrates. Collectively, these data indicate that vertebrate melanins share fundamental physiological roles in homeostasis via the scavenging and sequestering of metals and suggest that intimate links between melanin and metal metabolism in vertebrates have deep evolutionary origins.

fossil melanin | synchrotron X-ray fluorescence | soft tissue | taphonomy | metallome

Melanins are a family of widely expressed (1) and highly cross-linked (2) pigments derived from the oxidation of the amino acid tyrosine (3). In vertebrates, melanin is packaged as supermolecular aggregates (4) within micrometer-sized organelles termed melanosomes (or melanin granules) (5). Evidence of melanin and melanosomes in diverse fossils (reviewed in refs. 6 and 7) is forging a new paradigm in paleobiology, allowing inferences of the adaptive coloration and behavior of extinct taxa (8, 9) (although these interpretations are not without limitations) (5–7). In addition to studies of coloration sensu stricto [e.g., of melanin-based patterning (10), structural coloration, and melanosome diversity (9, 11, 12) in fossil feathers and of countershading in ancient vertebrates (8, 13–17)], recent studies have highlighted the chemical taphonomy of melanin (2, 15, 18, 19), the melanin metallome (20, 21), and the evolution of integumentary melanosomes (22). Recent evidence for nonintegumentary melanin (extracutaneous) (5) (i.e., from internal tissues, excluding the eyes) in extant vertebrates and fossil amphibians (23, 24) supports hypotheses that melanosomes may have broader functions beyond integumentary coloration (25). Internal melanin is implicated in protection against pollutants, free radicals, low temperatures, and in organ development and function (reviewed in ref. 23). Excepting a single study on amphibians (24), however, previous paleontological studies have considered primarily integumentary and ocular melanosomes, revealing aspects of their geometry (11, 22, 26, 27), chemistry (2, 19, 28, 29), and metal content (20, 30, 31). The phylogenetic distribution and evolutionary history of internal melanosomes, however, have not been evaluated systematically. This is essential to accurate interpretations of fossil melanosomes and for understanding the functional evolution of melanin through deep time.

Here, we report the anatomical distribution, abundance, geometry, melanin chemistry, and elemental inventory of melanosomes in tissues from 15 extant vertebrate taxa, coupled with data on the distribution, geometry, and chemistry of preserved melanosomes in fossils (Table 1). We extracted melanosomes from 243 tissue samples of extant vertebrates (Dataset S1 and *SI Appendix*) using a modified enzymatic melanosome extraction (EME) process (26) and sampled melanosome-rich soft tissues in fossils (Dataset S2). Melanin chemistry was analyzed for selected samples (Dataset S1) using alkaline hydrogen peroxide oxidation (AHPO) (4), a chemical assay used to quantify the concentration of melanin-specific molecular markers present in modern (32) and fossil (2) samples. The AHPO results are supported by Warthin–Starry staining of histological sections (Dataset S1), which produces diagnostic results for melanin (33) (*SI Appendix*). Scanning electron microscopy (SEM) and synchrotron rapid scanning X-ray fluorescence (SRS-XRF) were used to analyze the geometry and major-to-trace elemental chemistry, respectively, of extracted and fossil melanosomes (including, for SRS-XRF, analysis of whole untreated fossil specimens) (Dataset S2). For SRS-XRF, we analyzed the concentrations of 11 elements: phosphorous (P), sulfur (S), chlorine (Cl), potassium (K), calcium

Significance

Recent reports of nonintegumentary melanosomes in fossils hint at functions for melanin beyond color production, but the biology and evolution of internal melanins are poorly understood. Our results show that internal melanosomes are widespread in diverse fossil and modern vertebrates and have tissue-specific geometries and metal chemistries. Tissue-specific chemical signatures can persist in fossils despite some diagenetic overprint, allowing the reconstruction of internal soft-tissue anatomy in fossil vertebrates, and suggest that links between melanin and metal regulation have deep evolutionary origins in vertebrates.

Author contributions: V.R. and M.E.M. designed research; V.R., M.E.M., S.I., and K.W. performed research; S.M.W., S.I., and K.W. contributed new reagents/analytic tools; V.R., S.I., and K.W. analyzed data; and V.R. and M.E.M. wrote the paper.

The authors declare no conflict of interest.

This article is a PNAS Direct Submission. R.A.W. is a guest editor invited by the Editorial Board.

This open access article is distributed under Creative Commons Attribution-NonCommercial-NoDerivatives License 4.0 (CC BY-NC-ND).

[1]To whom correspondence may be addressed. Email: valentina.rossi@ucc.ie or maria.mcnamara@ucc.ie.

This article contains supporting information online at www.pnas.org/lookup/suppl/doi:10.1073/pnas.1820285116/-/DCSupplemental.

Published online August 19, 2019.

Table 1. List of extant and fossil specimens and techniques

Type	Class	Species name	Common name/museum no.	Technique
Extant	Amphibia	*Xenopus laevis*	African clawed frog	1,2,3,4,5
Extant	Amphibia	*Hymenochirus boettgerii*	Dwarf African clawed frog	2,3,4,5
Extant	Amphibia	*Cynops orientalis*	Fire-bellied newt	2,4,5
Extant	Reptilia	*Basiliscus basiliscus*	Brown basilisk	2,4,5
Extant	Reptilia	*Ctenosaura similis*	Black iguana	1,2,4,5
Extant	Reptilia	*Eublepharis macularius*	Leopard gecko	1,2,3,4,5
Extant	Reptilia	*Anolis carolinensis*	Green anole	2,3,4,5
Extant	Aves	*Taeniopygia guttata*	Zebra finch	2,3,4,5
Extant	Aves	*Lonchura oryzivora*	Java sparrow	2,4,5
Extant	Aves	*Scolopax rusticola*	Woodcock	1,2,3,4,5
Extant	Aves	*Troglodytes troglodytes*	European wren	1
Extant	Mammalia	*Mus musculus*	Brown mouse	1,2,3,4,5
Extant	Mammalia	*Oryctolagus cuniculus*	European rabbit	1,2,4,5
Extant	Mammalia	*Sus scrofa*	Domestic pig	1,2,3,4,5
Extant	Mammalia	*Ovis aries*	Domestic sheep	1,2,4,5
Fossil	Amphibia	*Pelophylax pueyoi*	NHML-R4999	4,5
Fossil	Amphibia	*Pelophylax pueyoi*	NHML-R4982	4,5
Fossil	Reptilia	Reptilia indet.	HMLDMe9018	4,5
Fossil	Mammalia	Chiroptera indet.	HMLDMe7069	4,5

1, alkaline hydrogen peroxide oxidation; 2, enzymatic melanin extraction; 3, histology; 4, scanning electron microscopy; 5, synchrotron rapid scanning X-ray fluorescence analysis.

(Ca), titanium (Ti), manganese (Mn), iron (Fe), nickel (Ni), copper (Cu), and zinc (Zn) (*SI Appendix*). ANOVA and linear discriminant analysis (LDA) tested for systematic variation in melanosome geometry and chemistry among tissues within each taxon.

Results

Internal Tissues of Extant Vertebrates Contain Melanin. Our results show that all modern tissues analyzed using AHPO ($n = 32$) (Fig. 1) contain pyrrole-2,3,5-tricarboxylic acid (PTCA) and pyrrole-2,3,4,5-tetracarboxylic acid (PTeCA) (2), which are diagnostic markers for eumelanin (EM) (4); analysis of tissue samples after hydroiodic acid (HI) analysis revealed the presence of 4-amino-3-hydroxyphenylalanine (4-AHP), a specific biomarker for pheomelanin (PM) (34), in all modern samples (note that none was detected in the fossil tissue from *Pelophylax pueyoi*) (Fig. 1 and Dataset S3). Extant amphibians and reptiles contained higher concentrations (>10 ng/mg) of melanin markers in internal organs, and, in particular, PTCA than extant birds and mammals (Fig. 1).

Except for the heart of the leopard gecko (*Eublepharis macularius*), all tissues analyzed ($n = 28$) stained positively for melanin (*SI Appendix*, Fig. S1). Analysis of histological sections supports the AHPO data: Internal organs in amphibians and reptiles contained more melanin than those in birds and mammals (mean area of tissue = 1.14 ± 1.66% [Amphibia]; 0.89 ± 1.79%

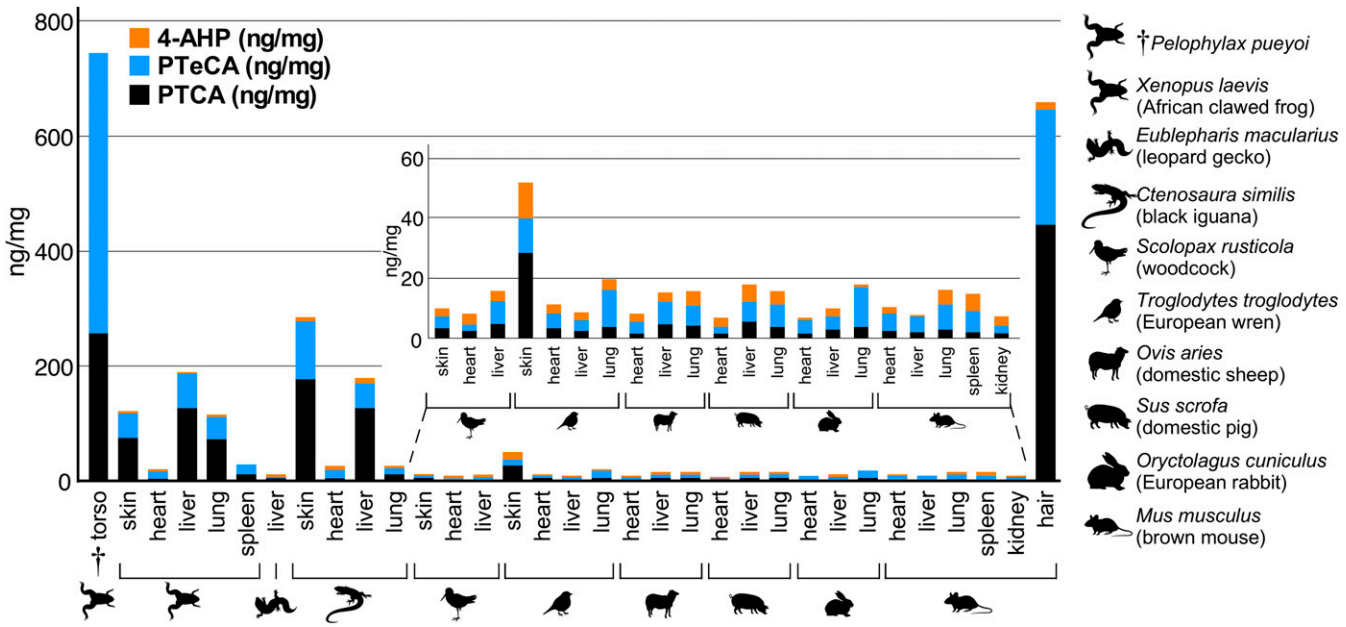


Fig. 1. Alkaline hydrogen peroxide oxidation (AHPO) and HI hydrolysis of extant and fossil tissues. All extant tissues analyzed contain pyrrole-2,3,5-tricaboxylic acid (PTCA) (a eumelanin marker) and 4-amino-3-hydroxyphenylalanine (4-AHP) (a pheomelanin marker). The fossil sample (†torso, *P. pueyoi*) contains PTCA and abundant pyrrole-2,3,4,5-tetracarboxylic acid (PTeCA) (a marker for diagenetically altered melanin), but no 4-AHP. *P. pueyoi* data from ref. 24.

[Reptilia]; 0.40 ± 0.68% [Aves]; 0.32 ± 0.33% [Mammalia]) (*SI Appendix* and Dataset S4). No tissue was consistently richer in melanin in all taxa. Excepting the dwarf African clawed frog (*Hymenochirus boettgerii*), within-taxon differences in the amount of melanin among tissues were statistically significant for all taxa (Dataset S5).

Following EME, most tissue samples (73%) (Dataset S1) yielded extracts that consist of near-pure isolates of melanosomes (*SI Appendix*, Figs. S2–S4; but see also *SI Appendix*, *Supplementary Text*). All measured melanosomes plotted within the morphospace defined previously for vertebrate integumentary melanosomes (22) (*SI Appendix*, Fig. S5). Scatter plots of melanosome geometry for each taxon showed considerable overlap in morphospace for melanosomes from different tissues (*SI Appendix*, Fig. S6 *A–H*). Differences in melanosome geometry between tissues were, however, statistically significant for all taxa (Datasets S6–S8) and were evident in box plots of melanosome length, width, and aspect ratio (Fig. 2 and *SI Appendix*, Figs. S7*A*–S14*A*) coupled with schematic representations of melanosome morphologies (*SI Appendix*, Figs. S7*B*–S14*B*; see also *SI Appendix*, *Supplementary Text*). The number of taxa for which it was possible to assess melanosome geometry in integumentary and nonintegumentary tissues varied among the vertebrate groups studied (amphibians = 2, reptiles = 4, birds = 1, mammals = 1). It is thus possible to discuss general phylogenetic trends in melanosome size and geometry only for amphibians and reptiles. In the amphibians analyzed, melanosomes from all tissues were similar in aspect ratio but differed in size; there was no clear trend for integumentary melanosomes to be larger or smaller than others (*SI Appendix*, Figs. S7 and S8). Similarly, in

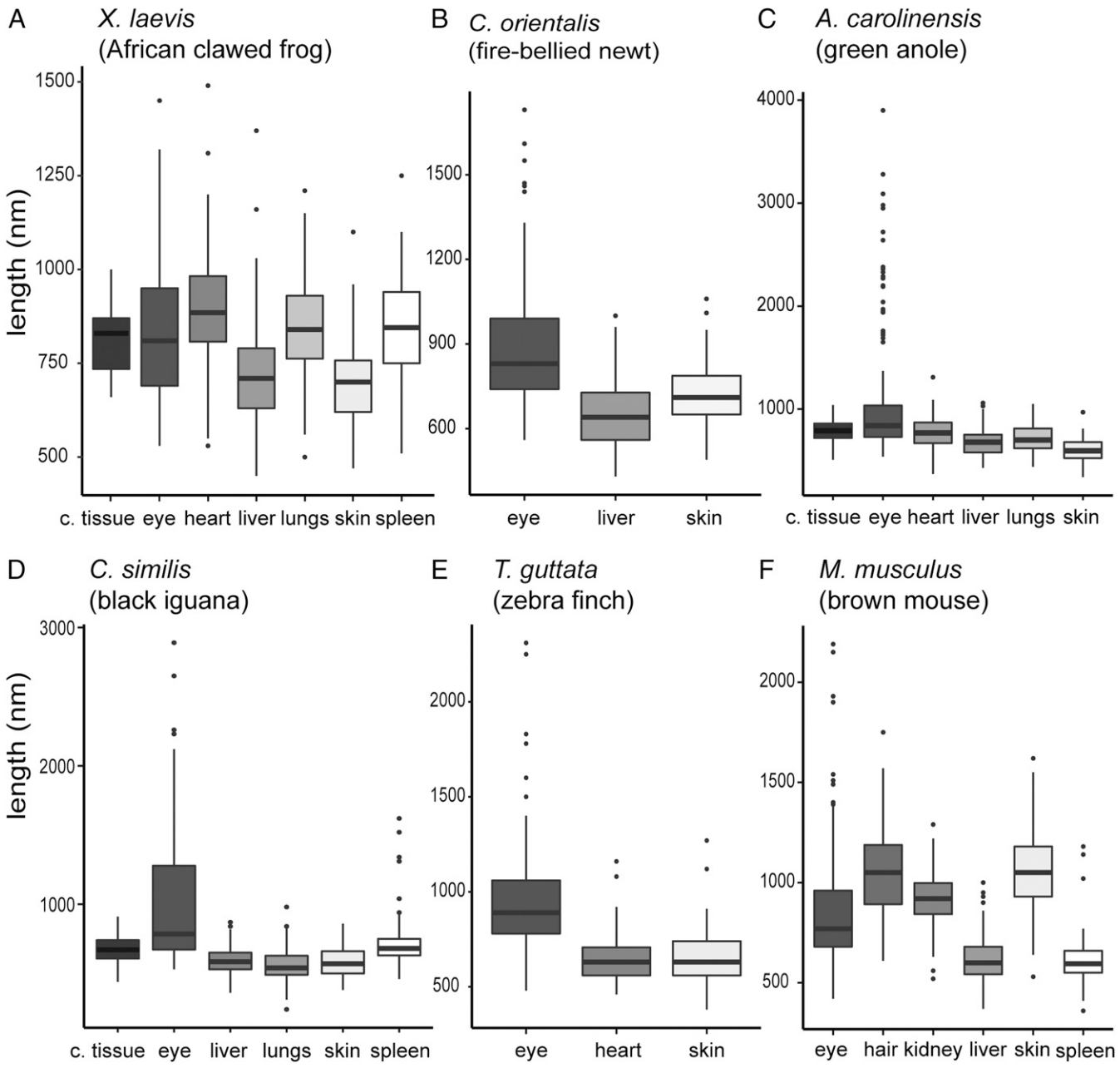


Fig. 2. Melanosome length for tissues in extant vertebrates. *A–F* show data for melanosome length in the eye, integumentary tissues and nonintegumentary tissues. The thick middle black line in each box plot is the median. c. tissue, connective tissue.

reptiles, melanosomes from most tissues were similar in aspect ratio but differed in size; integumentary melanosomes were usually smaller than nonintegumentary melanosomes (*SI Appendix*, Figs. S9–S12).

More subtle variations in melanosome geometry and size were evident within individual taxa. In the frog (*Xenopus laevis*) (Fig. 2*A* and *SI Appendix*, Fig. S7), melanosomes from the heart, lungs, connective tissue, and spleen were larger than those in the liver and skin. In the basilisk (*Basiliscus basiliscus*), melanosomes from the skin and spleen were smaller and had lower aspect ratios than those from connective tissue; liver melanosomes were intermediate in size and had a low aspect ratio (*SI Appendix*, Fig. S9). In the black iguana (*Ctenosaura similis*), melanosomes from the skin, lungs, and liver were smaller than those from the spleen and connective tissue; spleen melanosomes had higher aspect ratios than all others (*SI Appendix*, Fig. S10). In the green anole (*Anolis carolinensis*) and leopard gecko (*E. macularius*), skin melanosomes were smaller than, but had similar aspect ratio to, all others (*SI Appendix*, Figs. S11 and S12). In the zebra finch (*Taeniopygia guttata*) (Fig. 2*E*), heart melanosomes were similar in length (but not in aspect ratio) to skin melanosomes (*SI Appendix*, Fig. S13). In the brown mouse (*Mus musculus*), nonintegumentary melanosomes were usually smaller than integumentary melanosomes, except for the melanosomes from the kidneys (Fig. 2*F* and *SI Appendix*, Fig. S14).

Melanosomes Have Tissue-Specific Elemental Chemistries. We analyzed our SRS-XRF data on modern melanosomes (Dataset S9) using linear discriminant analysis (LDA), which is a multivariate statistical method that generates linear combinations of variables that best characterize variation among groups in a dataset (see *SI Appendix* for more details). LDA plots revealed that individual melanin extracts from different tissues and taxa differ in elemental chemistry (Fig. 3 and *SI Appendix*, Fig. S15). LDA biplots (circles in Fig. 3 and *SI Appendix*, Fig. S15) show that most of the chemical variation is driven by Ca, Fe, and, in some cases, Zn (*SI Appendix*). This tissue-specific variation was conserved at the class level and was enhanced by combining SRS-XRF and geometry data (Fig. 3 *A* and *B*). In amphibians (Fig. 3*A*), skin melanosomes were smaller (see also Fig. 2 *A* and *B* and *SI Appendix*, Figs. S7 and S8) and richer in Ca than nonintegumentary melanosomes. Liver melanosomes were usually slightly larger and were enriched in Fe relative to skin melanosomes. Lung melanosomes were larger and had less Fe and Ca than liver and skin melanosomes. Eye melanosomes were enriched in Ti. Similarly, in reptiles (Fig. 3*B* and *SI Appendix*, Figs. S9–S12), skin melanosomes were typically smaller and contained relatively less Fe and more Ca than melanosomes from internal organs. Heart melanosomes were larger than liver melanosomes. Eye- and connective-tissue melanosomes were relatively large and enriched in Zn and Ca. Geometry data are incomplete for birds and mammals; SRS-XRF data alone (*SI Appendix*, Fig. S15) can discriminate between melanosomes from different tissues in these groups. In birds (Fig. 3*C*), skin and eye melanosomes were rich in Ca relative to melanosomes from internal organs whereas melanosomes in the spleen were enriched in Fe and Ti relative to those in all other tissues. The chemospace plot for mammals shows more overlap among tissues relative to the other vertebrate groups. Lungs, liver,

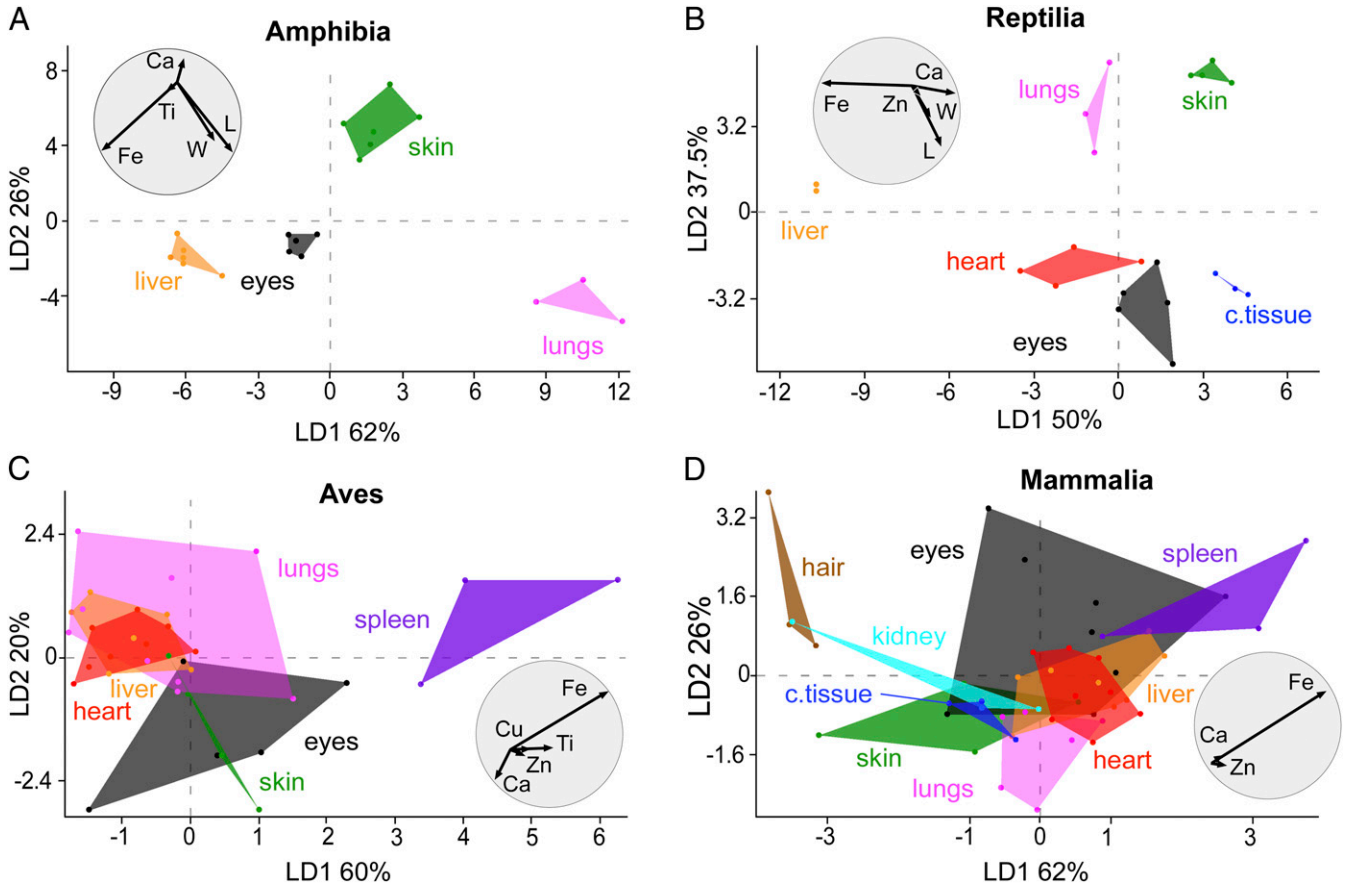


Fig. 3. Linear discriminant analysis (LDA) of geometry and elemental chemistry of melanosomes from extant vertebrates: Amphibia (*A*), Reptilia (*B*), Aves (*C*), Mammalia (*D*). Each LDA plot is accompanied by a biplot (grey circle) that shows the most discriminating variables contributing to the separation among groups. c. tissue, connective tissue; L, length; W, width.

and heart contained similar levels of Fe that are greater than those in the skin and less than those in the spleen (Fig. 3*D*). Individual mammalian taxa (*SI Appendix*, Figs. S15 *D* and *L*), however, showed clear separation in melanosome chemistry among tissues: for example, in the mouse (*M. musculus*) (*SI Appendix*, Fig. S15*D*), skin melanosomes were richer in Ca and Fe than those from hair and internal organs.

Fossilized Melanosome Films Can Define Anatomical Features in Fossil Vertebrates. We analyzed dark-colored, near-2D carbonaceous films that define soft tissues in a fossil tadpole (NHML4999; *P. pueyoi* [Libros]) (Fig. 4 *A* and *C*; samples 1 to 6), frog (NHML4892; *P. pueyoi* [Libros]) (Fig. 5 *A* and *I*; samples 7 to 9), bat (HMLD Me7069b; Chiroptera indet. [Messel]) (Fig. 5 *C* and *I*; samples 13 to 16), and reptile (HMLD Me9018; Reptilia indet. [Messel]) (Fig. 5 *E* and *I*; samples 10 to 12). SEM images revealed that almost all of these films comprise densely packed, 3D microbodies, often organized into size-specific layers (Fig. 5*I*, samples 9, 11a, and 11b; no melanosomes were observed in samples 10 and 12). As previously reported (24), where sufficiently large samples were available for AHPO analysis, results confirmed the presence of diagenetically altered melanin (pyrrole-2,3,4,5-tetracarboxylic acid [PTeCA]) (Fig. 1); the fossil structures were thus interpreted as preserved melanosomes. The high amount of melanin markers in the fossil samples (relative to fresh tissue samples) likely reflects high concentrations of melanin resulting from the decay and loss of associated lipids and proteins (28).

Melanosomes from different body regions of individual fossils differed significantly in geometry (*SI Appendix*, Figs. S16–S19 and Datasets S10–S12). Similar to extant taxa, melanosomes in fossil amphibians (*SI Appendix*, Figs. S16 and S17) were larger and had a lower aspect ratio than melanosomes in the fossil reptile (*SI Appendix*, Fig. S18). The fossil bat had the largest melanosomes; in the skin, melanosomes showed two distinct morphotypes (*SI Appendix*, Fig. S19, samples 13 and 16).

Chemistry of Fossilized Melanosomes Reveals Fossil Anatomy. XRF analyses of fossil specimens revealed striking partitioning of elements among anatomical structures defined by melanosomes (Figs. 4*B* and 5 *B* and *D*, *SI Appendix*, Figs. S20 and S21, and Dataset S13). The fossil soft tissues analyzed preserved exclusively three dimensionally preserved melanosomes; no secondary mineralization or associated organic matrix was apparent (Figs. 4*C* and 5*I*). The chemical data thus derive directly from the melanosomes and likely represent melanin-bound elements. Maps for Cu and Zn of the fossil tadpole NHML-R4999 (*P. pueyoi*, Libros) (Fig. 4) show that Zn (and, to a lesser extent, Cu) is concentrated in the eyespot, body outline, tail myomeres, and notochord. Cu is particularly concentrated within a distinct region in the anterior right part of the torso. Ti and, to a lesser extent, S are enriched in the eyespot, the body outline, and, especially, two regions in the central torso. Mn and Fe are enriched in a region on the left side of the central torso, the eyespot, and, for Mn only, the outline of the tail (see *SI Appendix* for more details).

The other fossils analyzed also showed striking chemical partitioning between melanosomes in the skin and internal tissues. In the fossil frog NHML-R4982 (Fig. 5 *A* and *B* and *SI Appendix*, Fig. S20), Cu and Zn were enriched in a region centered on the torso and pelvic girdle, and, in the case of Zn, the left eyespot and the body outline: that is, the skin. Similarly, in the fossil bat HMLD Me7069b (Fig. 5 *C* and *D* and *SI Appendix*, Fig. S21), Cu, Zn, and, to a lesser extent, Ti were enriched in one region below the rib cage (samples 14 and 15 in Fig. 5*C*). Ca was enriched in the wing patagia. Finally, in HMLD Me9018 (Reptilia indet., Messel) (Fig. 5 *E*–*H*), Ti, Fe, and Mn were enriched in the skin (sample 10 in Fig. 5*F*) and the torso (samples 11 and 12 in Fig. 5 *G* and *H*), but the skin was richer in Zn and Cu than the torso.

Linear Discriminant Analysis (LDA) plots of the SRS-XRF data for the fossil specimens revealed that individual regions of interest (ROIs) (*SI Appendix*, Fig. S22) analyzed have distinct elemental chemistries (Fig. 6). Further, the chemistry of the host matrix was usually different from that of the soft tissues, with

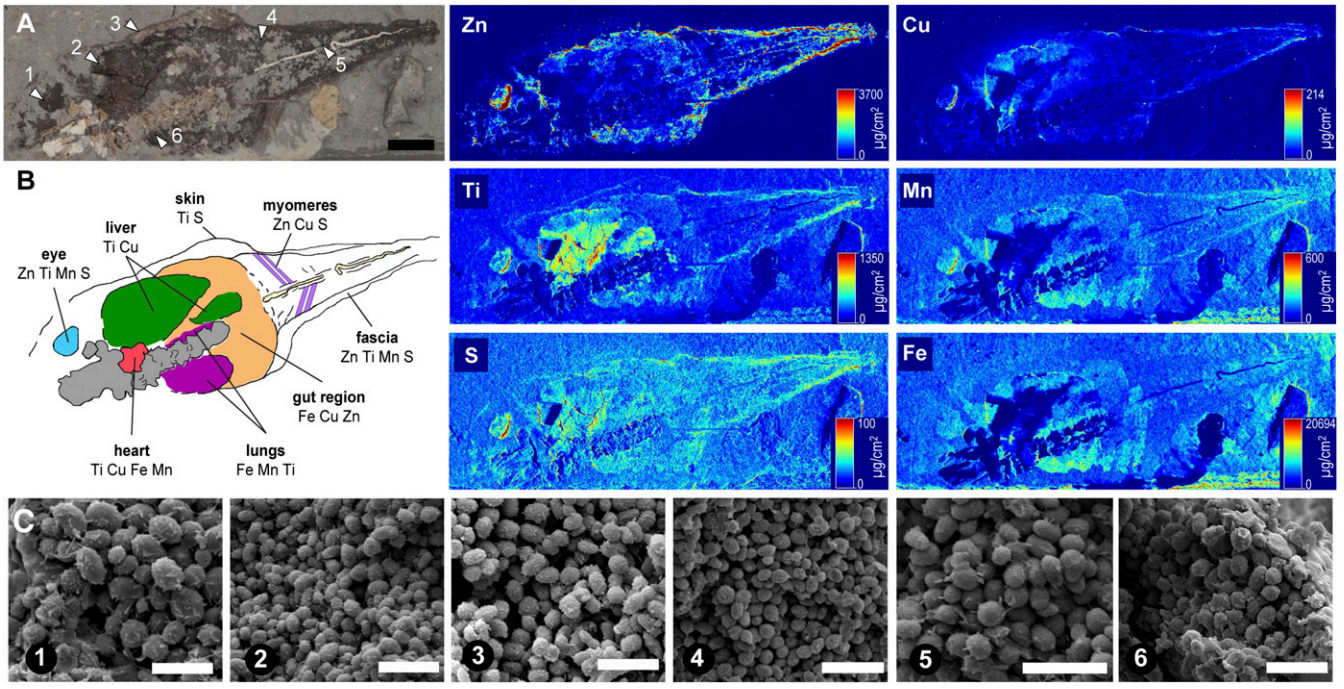


Fig. 4. Analysis of fossil tadpole NHML-R4999 (*P. pueyoi*, Libros). (*A*) Location of sampling points (arrowheads). (*B*) Interpretation of internal anatomy is based on the location, geometry, and chemistry (as shown in the SRS-XRF elemental maps for S, Ti, Mn, Fe, Cu, and Zn) of melanosomes from distinct regions. (*C*) Scanning electron micrographs of fossil melanosomes; numbers denote sampling points in *A*. (Scale bars: *A*, 10 mm; *C*, 2 μm.)

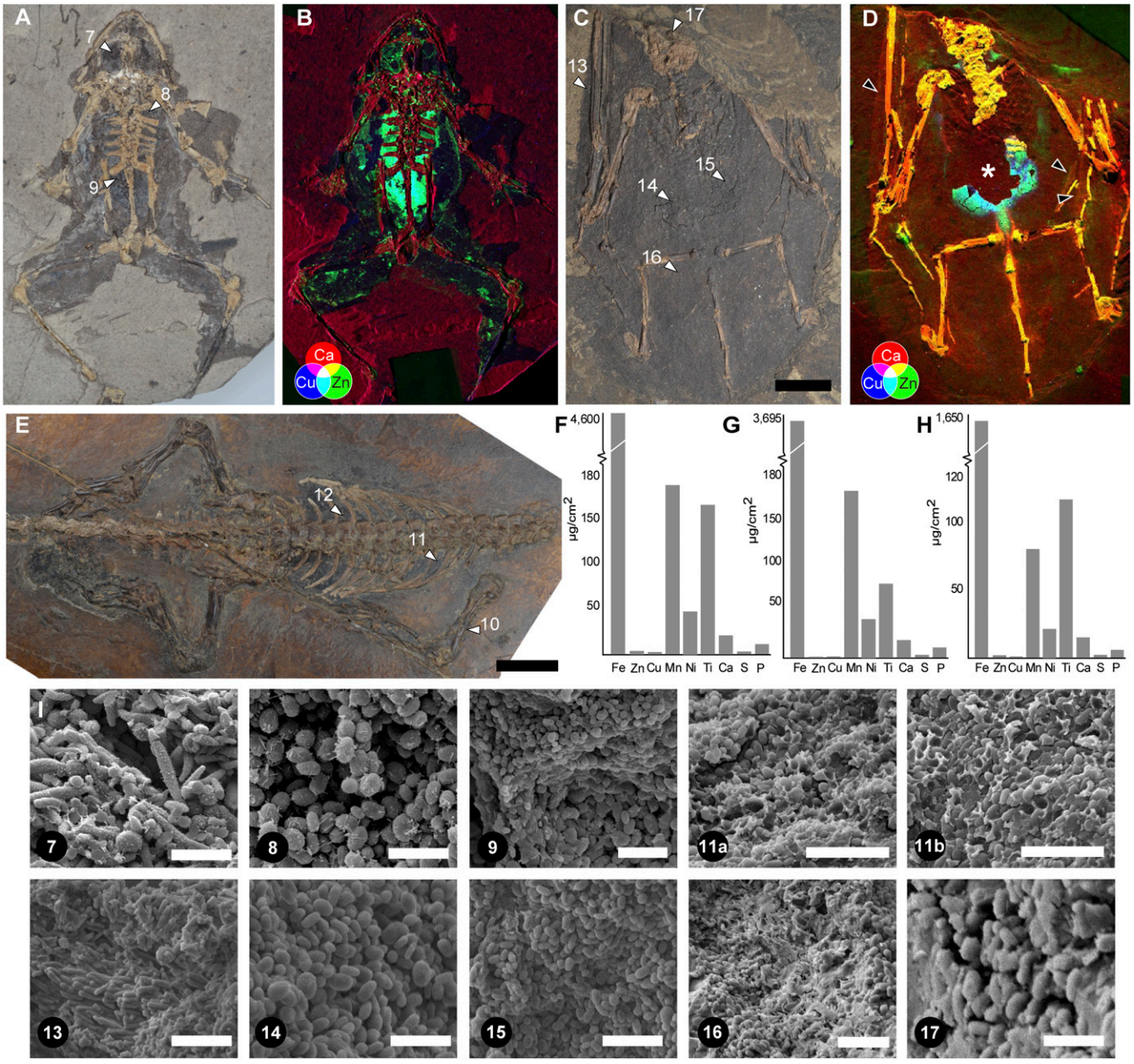


Fig. 5. Chemistry of preserved melanosomes in fossil vertebrates. False color SRS-XRF maps show Ca (red), Cu (blue), and Zn (green). White arrowheads, sampling points; black arrowheads (*D*), wing patagia. The asterisk (*) in *D* indicates local loss of tissue, revealing underlying sediment. (*A* and *B*) NHML-R4982; (*C* and *D*) HMLD Me7069b; (*E–H*) HMLD Me9018; (*F–H*) Concentrations of elements in samples 10, 11, and 12, respectively. (*I*) Scanning electron micrographs of fossil melanosomes; numbers denote sampling points shown in *A*, *C*, and *E*. No melanosomes were observed in the samples 10 and 12. (Scale bars: *A*, *C*, and *E*, 10 mm; *I*, 2 µm [excepting samples 11a and 11b, where the scale bar is 3 µm, and sample 16, where the scale bar is 5 µm].) (*A* and *B*) Image courtesy of Natural History Museum London, licensed under CC BY 4.0.

little or no overlap between the sediment and melanosome-rich regions in the LDA plots (Fig. 6 and Dataset S14). Chemical differences among melanosomes from different body regions were statistically significant (Datasets S15 and S16 and *SI Appendix*, *Supplementary Methods*).

Discussion

Our results expand on recent work (24) on nonintegumentary melanosomes in extant and fossil amphibians by demonstrating that the former are phylogenetically widespread in higher vertebrates, have a mixed eumelanin/pheomelanin composition, and have tissue-specific geometries and chemistries. Melanosome geometry differs significantly both among nonintegumentary melanosomes from different tissues and between these and the skin (Datasets S7 and S8). These differences are more readily visualized in box plots (Fig. 2 and *SI Appendix*, Figs. S7–S14) rather than scatter plots (*SI Appendix*, Fig. S6). We previously demonstrated that nonintegumentary melanosomes may impact reconstructions of melanin-based integumentary coloration in fossil amphibians (24). Here, we confirm that this issue applies to vertebrates more broadly and that nonintegumentary melanosome sources should be considered before inferring original melanin-based coloration in diverse fossil vertebrates. Moreover, our results do not show a correlation between geometry and melanin

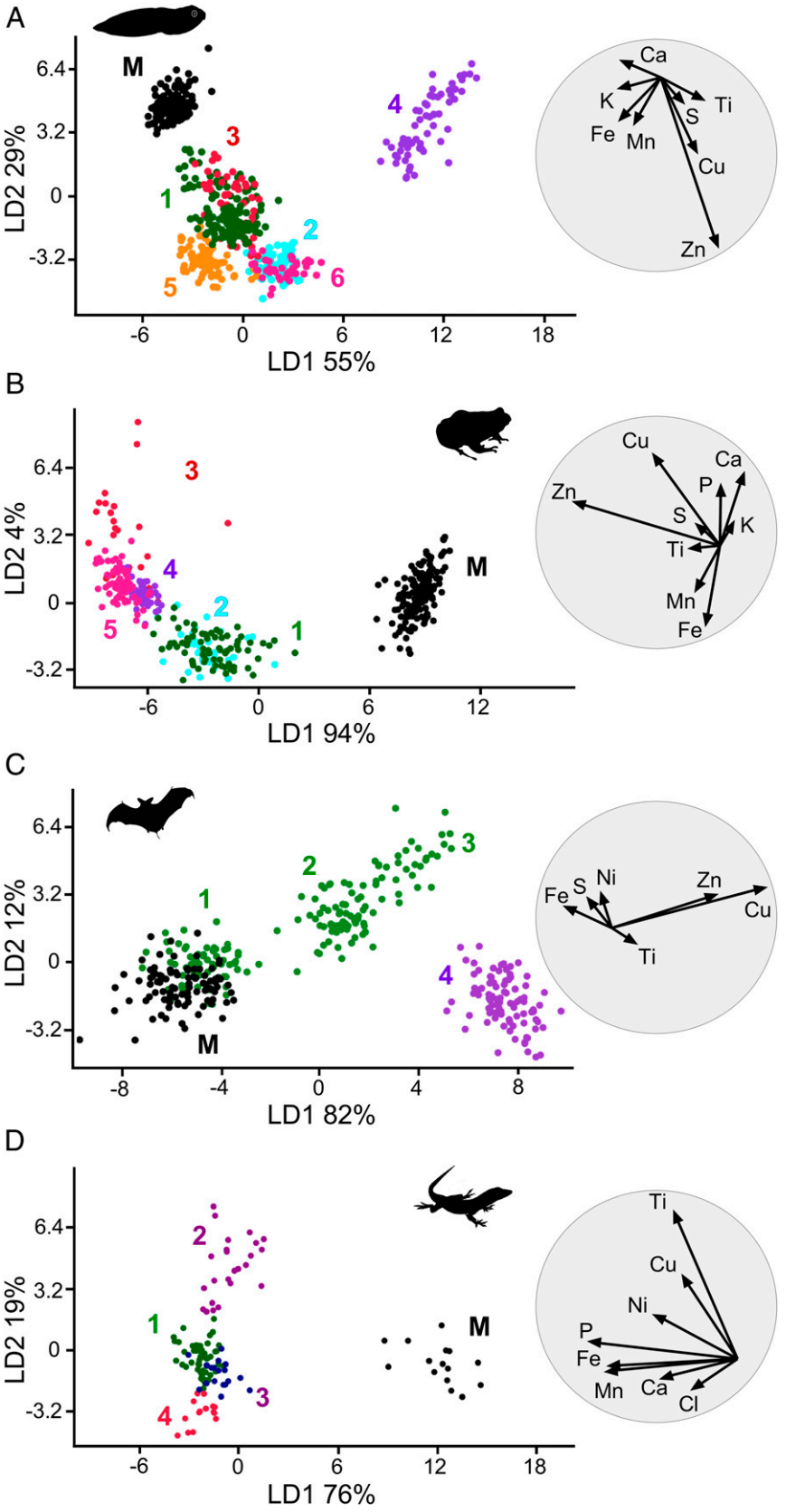


Fig. 6. Linear discriminant analysis of elemental chemistry of fossil melanosomes. (*A*) NHML-R4999 (*P. pueyoi*, Libros). (*B*) NHML-R4982 (*P. pueyoi*, Libros). (*C*) HMLD Me7069b (Chiroptera indet., Messel). (*D*) HMLD Me9018 (Reptilia indet., Messel). Each LDA plot is accompanied by a biplot (to the right). Numbers denote regions of interest (ROIs) (*SI Appendix*, Fig. S22) mapped using SRS-XRF; note that these numbers do not correspond to the sampling points for SEM analysis. M denotes sedimentary matrix (*A*–*C*) or resin (*D*). Colors that correspond to unequivocal organs: green, skin; cyan, eyespot; magenta, other soft tissue features.

chemistry (eumelanin vs. pheomelanin) of nonintegumentary melanosomes, unlike feathers from extant birds (21).

Nonintegumentary melanin, especially eumelanin, is particularly abundant in amphibians and reptiles, and the associated melanosomes in these taxa have less variable geometries than in birds and mammals (22) (*SI Appendix*, Fig. S6*I*). These patterns suggest high-level taxonomic controls on the biology of nonintegumentary melanin and melanosomes. Similar variations in the geometry of integumentary melanosomes in vertebrates are considered to reflect shifts in the melanocortin system, which is pleiotropically associated with metabolic rate (22, 35).

These observations, together with the common developmental origin of both melanin types from the neural crest (36), point to intimate and ancient links between the evolution of integumentary and nonintegumentary melanosomes. Indeed, the function and expression of melanocortin-1-receptor (*MC1R*) and agouti signaling protein (*ASIP*) in melanogenesis are highly conserved in vertebrates (23, 37) and tightly regulate phenotypic variation in melanin pigmentation (38) and physiology via pleiotropic effects (39). Our data, however, show no correlation between the amount of integumentary and nonintegumentary melanin in individual taxa; this is consistent with previous research (40) and suggests some decoupling of the selective forces promoting evolution of integumentary pigmentation and internal melanization (23).

Our discovery of tissue-specific chemical signatures associated with melanosomes in diverse vertebrates reveals pervasive and strong metal–melanin associations among vertebrates. The role of melanin in internal tissues of extant vertebrates is uncertain (41) but is hypothesized to relate to important physiological functions, such as immunity via the scavenging of reactive oxygen species and sequestration of toxic metal ions (23, 41) and the regulation of redox reactions (41), organ development and function, and hypoxemia (41). Further, there is increasing evidence that phenotypic expression of melanogenesis (i.e., integumentary patterning) may have evolved secondarily to other functions in metal ion exchange (42). The tissue-specific metal inventory of melanosomes reported in this study therefore likely relates to detoxification and metabolism (43) and may reflect the sequestration of toxic metabolic byproducts and/or a reservoir function for important redox-active metal ions (44, 45). The association of distinct metal signatures in melanosome-rich tissues in fossils is consistent with the hypothesis that the metal-mediated catalysis of biochemical processes has deep evolutionary origins (46).

Our discovery that preserved melanosomes can retain evidence of tissue-specific chemical signals in fossils has profound implications for interpretations of the internal anatomy of fossils. In the Libros tadpole NHML-R4999, no internal features are clearly defined by the melanosome film (except part of the margin of the notochord and tail myotomes). Based on anatomical comparisons with extant tadpoles (47), regions of the fossil that are enriched in different metals clearly map onto known anatomical features. The spatial partitioning of metals in the Libros tadpole (Fig. 4*B*) can thus be interpreted as follows. The skin is enriched in Ti and, to a lesser extent, S; collagenous tissues (internal fascia and perimysium) are enriched in Zn, Ti, S, and, to a lesser extent, Mn; and the eye (especially its posterior part) is enriched in Zn, Ti, Mn, and S. Within the body, the region rich in Ti and Cu corresponds to the position of the liver, and the region rich in Cu, Fe, and Mn immediately posterior to the cranial bones corresponds to the heart. The region close to the vertebrae that is rich in Fe and Ti corresponds to the position of the lungs. Preservation of spatially separated, chemically distinct regions in fossil soft tissues does not exclude the possibility that the elemental inventory in fossils has been altered during diagenesis (6) via, for example, geochemical processes (7) or mediation by bacterial metalloenzymes (48). Regardless, fossil melanosomes with distinct chemistries can clearly map onto discrete, known, anatomical structures, suggesting an underlying biological control. Critically, even if the preserved chemistry is not original, these features suggest that fossil melanosomes from different tissues preferentially associate with different metals during diagenesis. This confirms that a biological signal (that is at least indirect) can be preserved despite the effects of diagenesis.

Modern and fossil melanosomes differ in chemistry (Datasets S9 and S13). For example, in the African clawed frog (*X. laevis*), Fe, Ca, Zn, Cu, and, to a lesser extent, Ti are the principal metals associated with melanosomes; melanin is known to have a strong affinity for these metals (excepting Ti) (49). In contrast, melanosomes in the fossil amphibians are not enriched in Ca, but many tissues are associated with Zn, Ti, and Cu. Further, metal concentrations are typically higher in fossil melanosomes than in those extracted from fresh tissues; for example, in the fossil frog NHML-R4982, concentration of Ti varies between 5.7 $\mu g/cm^2$ to 22.2 $\mu g/cm^2$ (Dataset S13), whereas in the African clawed frog (*X. laevis*), Ti varies between 0.15 $\mu g/cm^2$ and 3.80 $\mu g/cm^2$ (Dataset S9). This, plus the widespread distribution of certain metals within individual fossil specimens, suggests partial chemical overprinting of the original biological signal.

The transformation of the metal content in fossil melanin and melanosomes during diagenesis may also control their preservation potential. The insolubility and recalcitrance of melanin have been related to its cross-linked polymeric structure (6, 17, 28). This cannot, however, be the sole taphonomic factor involved as evidence of melanin preserves in only some fossils. Transition metals are known to promote the formation of large molecular aggregates of melanin (50), especially at low pH (50). Fossil melanins can incorporate elements, notably S, during diagenesis, enhancing the preservation potential of melanin via increased cross-linking (51). Thus, the chelation of certain elements by melanin during diagenesis, controlled by local environmental factors (such as pH, element concentrations, and redox state), may influence the size of melanin aggregates and thus the preservation potential of fossil melanosomes. This is consistent with other hypotheses that metal–melanin associations may enhance the stability of fossil melanin (27) and the resistance of melanin to microbial decay (52, 53).

In conclusion, our study shows that the elemental chemistry of preserved melanosomes is a tool for interpreting the soft tissue anatomy of fossil vertebrates. By validating our approach using model taxa for which the anatomy is known in a closely related extant analog, we confirm its potential application in studies of other, more enigmatic taxa for which internal anatomy and/or phylogenetic affinities are less well constrained. Application of our systematic taxonomic approach in future studies of fossil vertebrates, integrating morphological and chemical analyses (6, 7), will elucidate the extent to which these chemical signatures are controlled by different biological and environmental factors. The tissue-specific elemental signatures of internal melanins reported here in diverse modern vertebrates show that specific metal–melanin interactions are conserved within different vertebrate groups. This, plus the survival of tissue-specific chemical inventories in fossils, suggests that vertebrate melanins share fundamental physiological roles in metal metabolism that have deep evolutionary origins.

Materials and Methods

Modern Specimens. We have complied with all relevant ethical regulations. Euthanasia of extant vertebrates was approved by the Health Products Regulatory Authority of Ireland via authorization AE19130-IO87.

Tissue samples ($n = 243$) were dissected and analyzed from 15 species of extant vertebrates for the enzymatic melanin extraction (EME). For *Sus scrofa*, *Ovis aries*, and *B. basiliscus*, tissues were available for only one specimen of each taxon. Where one or three individuals were used in the study, all were used for melanin extraction (Dataset S1). Where four individuals were used in the study, one was used for histology, and three were used for melanin extraction (Dataset S1). Some tissue samples could not be analyzed using all methods due to small size (Dataset S1); as a result, more

tissue samples were used for melanin extraction (n = 243) and SRS-XRF (n = 183) than for AHPO (n = 32) or histology (n = 28). *Troglodytes troglodytes* tissues were available only for AHPO analysis.

Fossil Specimens. Specimens were selected where soft tissues were preserved as a dark-colored, near-2D film. Specimens were from different depositional and diagenetic environments (Dataset S2). Institutional abbreviations are as follows: Hessisches Landesmuseum Darmstadt (HLMD) and Natural History Museum London (NHML).

Enzymatic Melanin Extraction. A total of 243 tissues samples were selected for study (3 replicates of each of 81 tissues). Tissues were dissected with sterile tools and processed immediately or stored at −80 °C before EME. Melanin was extracted using a modified version of the protocol in ref. 26. In brief, samples were treated with 9 cycles of solutions using 1,4-DTT (DTT), proteinase-K, and papain while incubated at 37.5 °C at 200 rpm for 9 d (*SI Appendix*).

Alkaline Hydrogen Peroxide Oxidation. Alkaline hydrogen peroxide oxidation is a unique chemical assay for melanin that produces diagnostic chemical markers (e.g., pyrrole-2,3,5-tricarboxylic acid [PTCA], pyrrole-2,3-dicarboxylic acid [PDCA], and pyrrole-2,3,4,5-tetracarboxylic acid [PTeCA], which are derived from the dihydroxyindole parent subunit of the melanin molecule) that allow identification and quantification of melanin in modern and fossil materials (2, 4). Freeze-dried samples (n = 32) of skin, heart, liver, lungs, connective tissue, spleen, kidney, and hair of extant taxa (9 to 17 mg) were homogenized in water with a Ten-Broeck homogenizer at a concentration of 10 mg/mL. Aliquots (200 μL) were dried in a dessicator and subjected to acid hydrolysis with 6 M HCl (0.5 mL) at 110 °C for 16 h (32). This acid hydrolysis removes proteins and small molecules that might interfere with the assay and thus increases specificity of the biomarkers (32). The resulting insoluble materials including melanin were collected by centrifugation and washed once with water as described previously (32). The residues were then subjected to alkaline hydrogen peroxide oxidation (AHPO) (4). Aliquots (100 μL) of tissue suspensions were also subjected to hydroiodic acid hydrolysis to analyze 4-amino-3-hydroxylphenylalanine (4-AHP), a specific biomarker for pheomelanin (34). A sample of soft tissues from a fossil frog from the Late Miocene Libros biota (MNCN 63776) was finely ground with a mortar and pestle and weighed. The powder was subjected to acid hydrolysis and AHPO analysis as above (4).

Histology. Tissues were dissected using sterile tools (n = 28), fixed with 75% ethanol, and embedded in paraffin wax. Histological sections (9 μm thick) were stained with the Warthin–Starry stain for melanin, which is considered more specific and sensitive to melanin than other histological stains (33) (*SI Appendix*). The percentage area of tissue occupied by melanin was calculated for each section by analyzing digital photographs using the Threshold Color plugin in ImageJ (54). Values cited here are mean values calculated from three representative images for each tissue. The values of the SDs are higher than the mean values; this is likely to happen when working with a small dataset showing a vast range of values.

Scanning Electron Microscopy. Fossil samples and melanin extracts were placed on aluminum stubs, coated with Au/Pd, and examined using an FEI Inspect F FE-SEM at an accelerating voltage of 5 to 10 kV. Extracts were screened using SEM, and only extracts containing pristine melanosomes (n = 95) (*SI Appendix*, Figs. S2–S4 and Dataset S1) were analyzed further. For each fossil sample and melanin extract, long and short axes of 50 melanosomes orientated perpendicular to line of sight were measured in ImageJ. Data were analyzed using R (55) and PAST (56).

Synchrotron Rapid-Scanning X-Ray Fluorescence. Rapid-scanning synchrotron-based X-ray fluorescence data were collected at the Stanford Synchrotron Radiation Lightsource using beam line 10-2. The incident X-ray energy was set to 11 keV using an Si (111) double crystal monochromator with the storage ring containing 500 mA in top-off mode at 3.0 GeV. A microfocused beam of 2 × 2 μm was provided by an Rh-coated Kirkpatrick–Baez mirror pair, pixel size 25 × 25 μm. The incident X-ray intensity was measured with a nitrogen-filled ion chamber. Specimens were mounted at 45° to the incident X-ray beam and were spatially rastered at 50 ms per pixel dwell time. The entire fluorescence spectrum was collected at each data point, and the intensity of fluorescence lines for selected elements (P, S, Cl, K, Ca, Ti, Mn, Fe, Ni, Cu, and Zn) was monitored using a silicon drift Vortex detector. Fluorescence intensities were corrected for detector deadtime and distance to allow comparison among samples. The concentrations of each element in μg/cm^2 were calibrated using NIST traceable thin film elemental standards. Data processing was performed using MicroAnalysis Toolkit software (57) (*SI Appendix*). Regions of interest for quantitative analysis were selected for each specimen. For each region of interest, raw pixel data, mean and SD values were calculated for the concentrations of each element. Differences in elemental concentrations between regions of interest were assessed using Linear Discriminant Analysis (LDA) in PAST. See *SI Appendix* for further details of SRS-XRF methods.

ACKNOWLEDGMENTS. We thank Roy Wogelius and 3 anonymous reviewers for their thoughtful and constructive comments. We thank Courtney Roach, Nick Edwards, Enrico Pirotta, Sharon Lynch, Babette Brooklar, Nick Hou, Chris Rogers, Naomi O'Reilly, Giliane Odin, Joe Tobin, Luke Harman, Carmel Hensey, Vince Lodge, Patricia Vernon, John Bainbridge, Liam Hayes, and Twomey's Butchers Macroom for assistance. This work was funded by European Research Council Starting Grant ERC-2014-StG-637691-ANICOLEVO (to M.E.M.). Use of the Stanford Synchrotron Radiation Lightsource, SLAC National Accelerator Laboratory, is supported by the US Department of Energy, Office of Science, Office of Basic Energy Sciences under Contract DE-AC02-76SF00515.

1. I. Galván, F. Solano, Melanin chemistry and the ecology of stress. *Physiol. Biochem. Zool.* **88**, 352–355 (2015).
2. K. Glass *et al.*, Direct chemical evidence for eumelanin pigment from the Jurassic period. *Proc. Natl. Acad. Sci. U.S.A.* **109**, 10218–10223 (2012).
3. P. A. Riley, Melanin. *Int. J. Biochem. Cell Biol.* **29**, 1235–1239 (1997).
4. S. Ito *et al.*, Usefulness of alkaline hydrogen peroxide oxidation to analyze eumelanin and pheomelanin in various tissue samples: Application to chemical analysis of human hair melanins. *Pigment Cell Melanoma Res.* **24**, 605–613 (2011).
5. J. J. Negro, C. Finlayson, I. Galván, Melanins in fossil animals: Is it possible to infer life history traits from the coloration of extinct species? *Int. J. Mol. Sci.* **19**, E230 (2018).
6. J. Lindgren *et al.*, Interpreting melanin-based coloration through deep time: A critical review. *Proc. Biol. Sci.* **282**, 20150614 (2015).
7. N. P. Edwards, P. L. Manning, R. A. Wogelius, Pigments through time. *Pigment Cell Melanoma Res.* **27**, 684–685 (2014).
8. J. Vinther *et al.*, 3D camouflage in an ornithischian dinosaur. *Curr. Biol.* **26**, 2456–2462 (2016).
9. D. Hu *et al.*, A bony-crested Jurassic dinosaur with evidence of iridescent plumage highlights complexity in early paravian evolution. *Nat. Commun.* **9**, 217 (2018).
10. Q. Li *et al.*, Plumage color patterns of an extinct dinosaur. *Science* **327**, 1369–1372 (2010).
11. Q. Li *et al.*, Reconstruction of *Microraptor* and the evolution of iridescent plumage. *Science* **335**, 1215–1219 (2012).
12. J. A. Clarke *et al.*, Fossil evidence for evolution of the shape and color of penguin feathers. *Science* **330**, 954–957 (2010).
13. C. M. Brown *et al.*, An exceptionally preserved three-dimensional armored dinosaur reveals insights into coloration and cretaceous predator-prey dynamics. *Curr. Biol.* **27**, 2514–2521.e3 (2017).
14. F. M. Smithwick, R. Nicholls, I. C. Cuthill, J. Vinther, Countershading and stripes in the theropod dinosaur *Sinosauropteryx* reveal heterogeneous habitats in the early cretaceous jehol biota. *Curr. Biol.* **27**, 3337–3343.e2 (2017).
15. M. E. McNamara *et al.*, Reconstructing carotenoid-based and structural coloration in fossil skin. *Curr. Biol.* **26**, 1075–1082 (2016).
16. S. E. Gabbott *et al.*, Pigmented anatomy in Carboniferous cyclostomes and the evolution of the vertebrate eye. *Proc. Biol. Sci.* **283**, 20161151 (2016).
17. J. Lindgren *et al.*, Skin pigmentation provides evidence of convergent melanism in extinct marine reptiles. *Nature* **506**, 484–488 (2014).
18. J. Lindgren *et al.*, Biochemistry and adaptive colouration of an exceptionally preserved juvenile fossil sea turtle. *Sci. Rep.* **7**, 13324 (2017).
19. C. Colleary *et al.*, Chemical, experimental, and morphological evidence for diagenetically altered melanin in exceptionally preserved fossils. *Proc. Natl. Acad. Sci. U.S.A.* **112**, 12592–12597 (2015).
20. R. A. Wogelius *et al.*, Trace metals as biomarkers for eumelanin pigment in the fossil record. *Science* **333**, 1622–1626 (2011).
21. N. P. Edwards *et al.*, Elemental characterisation of melanin in feathers via synchrotron X-ray imaging and absorption spectroscopy. *Sci. Rep.* **6**, 34002 (2016).
22. Q. Li *et al.*, Melanosome evolution indicates a key physiological shift within feathered dinosaurs. *Nature* **507**, 350–353 (2014).
23. S. Dubey, A. Roulin, Evolutionary and biomedical consequences of internal melanins. *Pigment Cell Melanoma Res.* **27**, 327–338 (2014).
24. M. E. McNamara *et al.*, Non-integumentary melanosomes can bias reconstructions of the colours of fossil vertebrates. *Nat. Commun.* **9**, 2878 (2018).
25. J. Vinther, A guide to the field of palaeo colour: Melanin and other pigments can fossilise: Reconstructing colour patterns from ancient organisms can give new insights to ecology and behaviour. *Bioessays* **37**, 643–656 (2015).

26. Y. Liu *et al*., Comparison of the structural and physical properties of human hair eumelanin following enzymatic or acid/base extraction. *Pigment Cell Res.* **16**, 355–365 (2003).
27. Y. Pan *et al*., Molecular evidence of keratin and melanosomes in feathers of the Early Cretaceous bird *Eoconfuciusornis*. *Proc. Natl. Acad. Sci. U.S.A.* **113**, E7900–E7907 (2016).
28. J. Lindgren *et al*., Molecular preservation of the pigment melanin in fossil melanosomes. *Nat. Commun.* **3**, 824 (2012).
29. T. Clements *et al*., The eyes of *Tullimonstrum* reveal a vertebrate affinity. *Nature* **532**, 500–503 (2016).
30. N. P. Edwards *et al*., Infrared mapping resolves soft tissue preservation in 50 million year-old reptile skin. *Proc. Biol. Sci.* **278**, 3209–3218 (2011).
31. V. M. Egerton *et al*., The mapping and differentiation of biological and environmental elemental signatures in the fossil remains of a 50 million year old bird. *J. Anal. At. Spectrom.* **30**, 627–634 (2015).
32. S. Ito *et al*., Acid hydrolysis reveals a low but constant level of pheomelanin in human black to brown hair. *Pigment Cell Melanoma Res.* **31**, 393–403 (2018).
33. N. Joly-Tonetti, J. I. D. Wibawa, M. Bell, D. Tobin, Melanin fate in the human epidermis: A reassessment of how best to detect and analyse histologically. *Exp. Dermatol.* **25**, 501–504 (2016).
34. K. Wakamatsu, S. Ito, J. L. Rees, The usefulness of 4-amino-3-hydroxyphenylalanine as a specific marker of pheomelanin. *Pigment Cell Res.* **15**, 225–232 (2002).
35. C. M. Eliason, J. A. Clarke, Metabolic physiology explains macroevolutionary trends in the melanic colour system across amniotes. *Proc. Biol. Sci.* **285**, 20182014 (2018).
36. C. D. Faraco, S. A. Vaz, M. V. Pástor, C. A. Erickson, Hyperpigmentation in the Silkie fowl correlates with abnormal migration of fate-restricted melanoblasts and loss of environmental barrier molecules. *Dev. Dyn.* **220**, 212–225 (2001).
37. J. K. Hubbard, J. A. C. Uy, M. E. Hauber, H. E. Hoekstra, R. J. Safran, Vertebrate pigmentation: From underlying genes to adaptive function. *Trends Genet.* **26**, 231–239 (2010).
38. Y. X. C. Bourgeois *et al*., A novel locus on chromosome 1 underlies the evolution of a melanic plumage polymorphism in a wild songbird. *R. Soc. Open Sci.* **4**, 160805 (2017).
39. A. Roulin, Melanin-based colour polymorphism responding to climate change. *Glob. Change Biol.* **20**, 3344–3350 (2014).
40. I. Galván, A. P. Møller, J. Erritzøe, Testicular melanization has evolved in birds with high mtDNA mutation rates. *J. Evol. Biol.* **24**, 988–998 (2011).
41. F. Solano, Melanins: Skin pigments and much more—types, structural models, biological functions, and formation routes. *New J. Sci.* **2014**, 1–28 (2014).
42. J. M. Wood *et al*., What's the use of generating melanin? *Exp. Dermatol.* **8**, 153–164 (1999).
43. A. Jakimska, P. Konieczka, K. Skóra, J. Namieśnik, Bioaccumulation of metals in tissues of marine animals, part I: The role and impact of heavy metals on organism. *Pol. J. Environ. Stud.* **20**, 1127–1146 (2011).
44. C. Andreini, I. Bertini, G. Cavallaro, G. L. Holliday, J. M. Thornton, Metal ions in biological catalysis: From enzyme databases to general principles. *J. Biol. Inorg. Chem.* **13**, 1205–1218 (2008).
45. M. L. Bender, Metal ion catalysis of nucleophilic organic reactions in solution. *Adv. Chem. Ser.* **37**, 19–36 (1962).
46. M. Kleczkowski, M. Garncarz, The role of metal ions in biological oxidation–The past and the present. *Pol. J. Vet. Sci.* **15**, 165–173 (2012).
47. R. W. McDiarmid, R. Altig, *Tadpoles: The Biology of Anuran Larvae* (University of Chicago Press, Chicago, 1999), 458 pp.
48. D. W. Choi *et al*., Spectral and thermodynamic properties of Ag(I), Au(III), Cd(II), Co(II), Fe(III), Hg(II), Mn(II), Ni(II), Pb(II), U(IV), and Zn(II) binding by methanobactin from *Methylosinus trichosporium* OB3b. *J. Inorg. Biochem.* **100**, 2150–2161 (2006).
49. L. Hong, J. D. Simon, Current understanding of the binding sites, capacity, affinity, and biological significance of metals in melanin. *J. Phys. Chem. B* **111**, 7938–7947 (2007).
50. J. M. Gallas, K. C. Littrell, S. Seifert, G. W. Zajac, P. Thiyagarajan, Solution structure of copper ion-induced molecular aggregates of tyrosine melanin. *Biophys. J.* **77**, 1135–1142 (1999).
51. M. E. McNamara, B. E. van Dongen, N. P. Lockyer, I. D. Bull, P. J. Orr, Fossilization of melanosomes via sulfurization. *Palaeontology* **59**, 337–350 (2016).
52. H. E. Barden *et al*., Morphological and geochemical evidence of eumelanin preservation in the feathers of the Early Cretaceous bird, *Gansus yumenensis*. *PLoS One* **6**, e25494 (2011).
53. P. L. Manning *et al*., Synchrotron-based chemical imaging reveals plumage patterns in a 150 million year old early bird. *J. Anal. At. Spectrom.* **28**, 1024 (2013).
54. C. A. Schneider, W. S. Rasband, K. W. Eliceiri, NIH Image to ImageJ: 25 years of image analysis. *Nat. Methods* **9**, 671–675 (2012).
55. R Core Team, R: A Language and Environment for Statistical Computing (Version 1.0.143). http://www.r-project.org/. Accessed 1 April 2016.
56. Ø. Hammer, D. A. T. Harper, P. D. Ryan, Paleontological Statistics Software: Package for Education and Data Analysis. 9 (Version 3.12, Øyvind Hammer, Natural History Museum, University of Oslo, Oslo, Norway, 2001).
57. S. M. Webb, The microAnalysis toolkit: X-ray fluorescence image processing software. *AIP Conf. Proc.* **1365**, 196–199 (2010).